Oxygen Evolution Reaction of Co-Mn-O Electrocatalyst Prepared by Solution Combustion Synthesis

Kyoung Ryeol Park [1] , **Jae Eun Jeon [1]** , **Ghulam Ali [2]** , **Yong-Ho Ko [3]** , **Jaewoong Lee [3]** , **HyukSu Han [4],*** and **Sungwook Mhin [3],***

[1] Department of Materials Science and Engineering, Hanyang University, Seoul 04763, Korea; nebula9938@kitech.re.kr (K.R.P.); jaeeun00@kitech.re.kr (J.E.J.)
[2] Department of Physics, University of the Punjab, Lahore 54590, Pakistan; ghulamali143@gmail.com
[3] Korea Institute of Industrial Technology, Gaetbeol-ro 156, Yeonsu-gu, Incheon 21999, Korea; yonghoko@kitech.re.kr (Y.H.K.); woong428@kitech.re.kr (J.L.)
[4] Department of Materials Science and Engineering, Hongik University, Sejong-ro 2639, Korea
* Correspondence: hhan@hongik.ac.kr (H.H.); hyeleci@kitech.re.kr (S.M.); Tel.: +82-31-8084-8641 (S.M.); Fax: +82-31-8084-8603 (S.M.)

Abstract: High-performance oxygen evolution reaction (OER) electrocatalysts are needed to produce hydrogen for energy generation through a carbon-free route. In this work, the solution combustion synthesis (SCS) method was employed to synthesize mixed phases of Co- and Mn-based oxides, and the relationships between the crystalline structure and the catalytic properties in the mixed phases were established. The mixed phases of Co- and Mn-based oxides shows promising OER properties, such as acceptable overpotential (450 mV for $10\,\mathrm{mA\cdot cm^{-2}}$) and Tafel slope ($35.8\,\mathrm{mV\cdot dec^{-1}}$), highlighting the use of the mixed phases of Co- and Mn-based oxides as a new efficient catalysts for water splitting. Electronic structure of the mixed phases of Co- and Mn based oxides is studied in detail to give insight for the origin of high catalytic activities. In addition, excellent long-term stability for OER in alkaline media is achieved for the mixed phase of Co- and Mn based oxides.

Keywords: cobalt manganese oxide; solution combustion synthesis; electrocatalyst; oxygen evolution reaction; water splitting

1. Introduction

Since the 1980s, when solution combustion synthesis (SCS) was invented, various nanoscale materials have been developed via SCS for a wide range of applications, such as in fields involving energy conversion, optical devices, catalysts, batteries, and supercapacitors [1–6]. SCS begins with the preparation of a homogeneous solution with precursors, including a suitable oxidizer and a fuel, which can allow an exothermic chemical reaction [7]. The oxidizer is selected on the basis of its solubility for a specific solvent at a certain decomposition temperature. The ideal fuel, as a source of carbon and hydrogen, should have a high solubility in the solvent and a low decomposition temperature, so it can facilitate the homogeneous mixing of metal cations in the solution [8,9]. During combustion synthesis, dehydration and thermal decomposition of the precursors occur, followed by a couple of redox exothermic reactions between oxidizer and fuel, which can yield uniform solid products with a large amount of gases [7].

Formation of the final products can be controlled by the kinetics of a chemical reaction during SCS. SCS, as a one-step process, results in the formation of desired crystalline nanomaterials but can give different types of materials on further heat treatment (i.e., calcination) to form the desired material [10].

In other words, SCS parameters such as the maximum temperature, heating rate, cooling rate, and processing time determine the equilibrium state of the final product. Mixed materials can be formed as multiphase nanoscale materials or partially oxidized materials. From a practical viewpoint, mixed materials can be utilized for different applications as catalysts, owing to their structural flexibility, more randomly oriented bonding, and high number of active sites originating from unstable surface energy states [11,12].

Among various oxides studied so far, Co- and Mn-based materials are promising high-performance oxygen evolution reaction (OER) electrocatalysts. Cations with mixed valence states, i.e., +2 to +3 for Co and +2 to +4 for Mn and a perturbed distribution of cations lead to flexible electronic configurations of the materials, resulting in high conductivity, and thus, high catalytic activity [13,14]. Our recent report on the synthesis of $(Co_xMn_{3-x})O_4$ (CMO) via SCS suggests that the crystal structure of CMO depends on the chemical composition after calcination at a relatively low temperature (~800 °C) according to the following chemical reaction [15]:

$$(3 - x) (Mn(NO_3)_2 + xCo(NO_3)_2 \cdot 6H_2O + C_6H_8O_7 + C_2H_6O_2 \rightarrow \text{mixed materials} \rightarrow$$
$$(Co_xMn_{3-x})O_4 + 8CO_2 + 13H_2O + 3N_2 \tag{1}$$
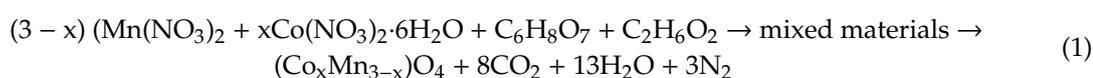
However, crystallographic information and related catalytic properties on the mixed phases of Co- and Mn-based materials are still lacking, but they can be crucial in revealing the formation mechanism of formation of spinel CMO. Furthermore, different types of materials are expected to show unusual catalytic activities depending on the mixed phases. Therefore, it is worthwhile to investigate the catalytic performance of the mixed materials. Herein, we report a systematic study of the crystallographic information and OER properties of mixed materials prepared via SCS. Electrochemical characterization revealed the relationship between the Co content and the OER performance of the mixed materials.

2. Results and Discussion

The average particle size of all samples was approximately 400 nm, which was determined from SEM images of the samples Figure 1. Figure 2 shows representative EDX mapping of mixed materials (Co = 1.2, 2.4, and 2.7). EDX elemental mapping indicates that Co and Mn were homogeneously distributed in the powder when the Co content was 1.2. However, segregation of Co and Mn was observed in the mixed materials with Co contents of 2.4 and 2.7, which implies inhomogeneous distribution of Co and Mn after SCS at Co contents higher than 2.4. However, oxygen was homogeneously distributed over the powders regardless of the Co content. As shown in Figure 3a, the mixed phases with Co = 1.2 prepared by SCS showed tetragonal spinel $CoMn_2O_4$ with small amounts of Co_3O_4 and MnO, while Co_3O_4 and CoO were mainly observed with increase in the Co contents up to Co = 2.7. XRD patterns of the mixed materials with Co = 2.4 were indexed with Co_3O_4 and CoO, but peak overlapping between 36.5° (left shoulder) and 36.8° (center) indicated that a partial solid solution reaction occurred leading to the formation of spinel CMO, as shown in Figure 3b. Considering the same processing parameters for the formation of mixed materials except for different Co contents, it is likely that the formation energy of spinel CMO increases with increasing Co content, as was evidenced by segregation of Co and Mn at Co contents higher than 2.4, as seen in Figure 2. Notably, peak positions shifted to higher 2 θ angles with increase in the Co content, as shown in Figure 3b, which indicates that greater incorporation of smaller Co ions decreased the lattice parameters of the mixed materials to promote the formation of the cubic spinel structure at Co = 2.4 and 2.7 [16]. Raman spectra for mixed materials in Figure 4 are also in agreement with the EDX and XRD results. In comparison to with the Raman spectra of Co_3O_4, different activated modes were observed for the mixed materials with Co = 1.2, which could be assigned to the 6 vibrational modes of tetragonal spinel $CoMn_2O_4$ [17]. The peaks at 180, 320, 372, 495, 585, and 664 cm^{-1} in the spectra of Co = 1.2 are due to the tetragonal spinel structure of $CoMn_2O_4$ [18]. Broadened Raman peaks at 180 cm^{-1}, between 320 and 370 cm^{-1}, and between 495 and 585 cm^{-1} can be attributed to the low crystallinity and nanosized grain of the

mixed materials with Co = 1.2. The Raman peaks of the mixed materials shifted slightly to higher frequencies with increase in the Co content, owing to changes in the cation–anion bonds in the lattice constriction of Co_3O_4 [17]. In particular, the most significant shift to a lower frequency was observed for the A_{1g} reflection, from 690 to 664 cm^{-1}, for the octahedral cation sites on the substitution of Co cations with Mn cations. The Raman peaks of CoO located at 484 and 691 cm^{-1} overlapped with those of Co_3O_4, which made it difficult to separate the cobalt oxide signals [19,20]. With increase in the Co content to values higher than Co = 2.4, five Raman activated modes ($A_{1g} + E_g + 3F_{2g}$) of the cubic spinel Co_3O_4 phase became obvious, while the characteristic peaks of Mn_3O_4 diminished. The characteristic peaks of A_{1g} and F_{2g} symmetry at 693 cm^{-1} and 196 cm^{-1} can be attributed to the octahedral CoO_6 and tetragonal CoO_4, respectively. Furthermore, three peaks at 484, 522, and 622 cm^{-1} could be assigned to the E_g, F_{2g}, and F_{2g} symmetry, respectively, which were related to the Raman vibration of Co^{3+}-O^{2-} and Co^{2+}-O^{2-} at tetragonal and octahedral sites [21]. Based on EDX mapping, XRD, and Raman spectroscopy results, segregation of Co and Mn at higher Co contents above Co = 2.4 made the formation of spinel CMO difficult, as evidenced by the formation of Co- rich phases such as Co_3O_4 and CoO and amorphous Mn phases at higher Co contents, while the formation of tetragonal spinel CMO was preferred for comparatively homogeneous distribution of Co and Mn at low Co contents (Co = 1.2). As reported previously, the mixed materials transformed to tetragonal or cubic spinel CMOs depending on the Co content at a high temperature (~800 °C) [15]. It is proposed that incorporation of Co from Co_3O_4 and Mn from MnO into tetragonal CMO occurs, resulting in the formation of highly crystalline tetragonal CMO at low Co contents (Co = 1.2), while CoO and amorphous Mn phases can react with cubic spinel Co_3O_4 for the formation of cubic CMO at high Co contents (Co = 2.4 and 2.7) during calcination. Transformation of tetragonal spinel to the cubic form with increase in the Co content indicates a different formation mechanism during SCS, i.e., tetragonal spinel $(Co_xMn_{3-x})O_4$ to cubic spinel Co_3O_4, suggesting that the formation energy of tetragonal spinel $(Co_xMn_{3-x})O_4$ is lower than that of cubic spinel $(Co_xMn_{3-x})O_4$ during SCS.
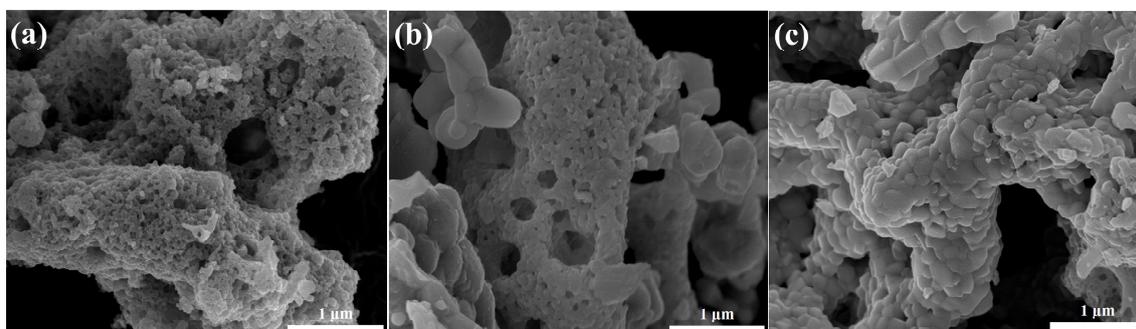
Figure 1. SEM images for Co- and Mn-based materials with (**a**) Co 1.2; (**b**) Co 2.4; and (**c**) Co 2.7.
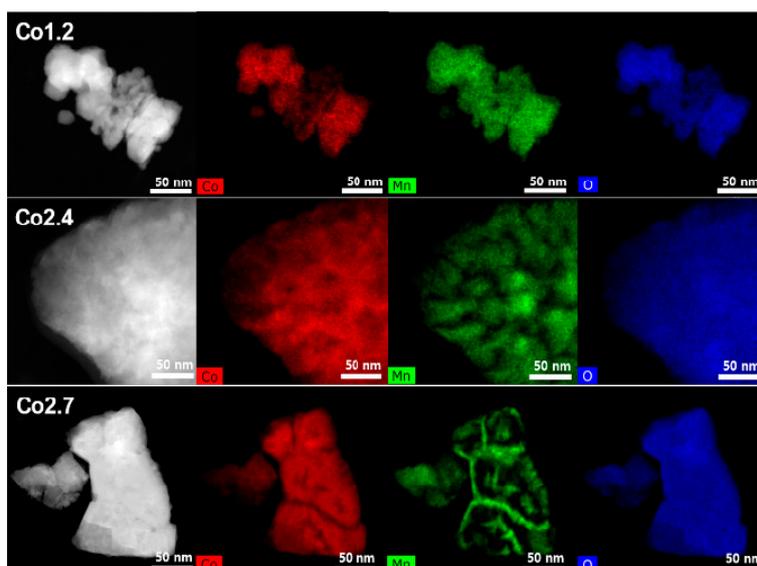
Figure 2. TEM-EDS mapping images for Co, Mn, and O in the mixed phases of Co- and Mn-based materials with Co = 1.2, 2.4, and 2.7.
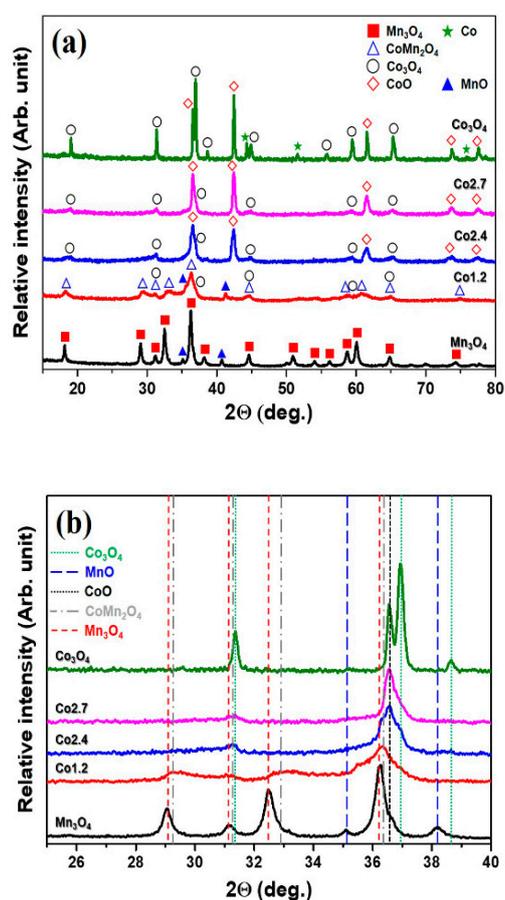
Figure 3. (**a**) XRD patterns of Co- and Mn-based the mixed phase materials (Co = 0, 1.2, 2.4, 2.7, and 3) and (**b**) enlarged XRD patterns in 2 θ range of 25–40°.
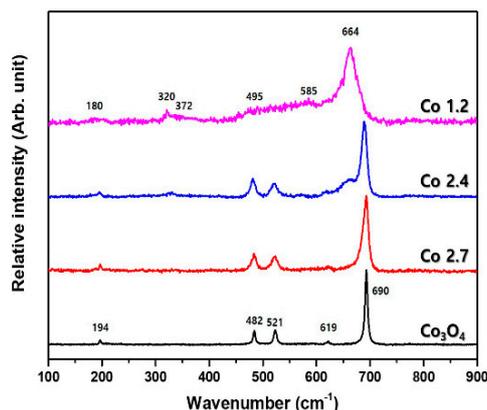
Figure 4. Raman spectra of Co- and Mn-based the mixed phase materials with different Co contents (Co = 1.2, 2.4, 2.7, and 3).

In order to probe local structural differences between mixed materials with Co = 1.2, 2.4, and 2.7, we conducted X-ray absorption near edge structure (XANES) spectroscopy. XANES spectroscopy is a powerful technique to probe both crystalline and amorphous materials, as it does not necessarily require long-range order. Figure 5a shows the Co K-edge XANES spectra of mixed materials with Co = 1.2, 2.4, and 2.7, along with reference Co^0, Co^{2+}, and Co^{3+} spectra. The Co- edge spectra show pre-edge peaks that are magnified in the inset of Figure 5a. Two pre-edge peaks (A & B) can be observed in the XANES spectrum of the mixed material with Co = 1.2. The split of the pre-edge peaks in the mixed material with Co = 1.2 was due to mixed phases of Co- rich cubic and tetragonal structures, which could be Co_3O_4 and tetragonal spinel CMO. The main edge peak was found to overlap with the Co^{2+} reference in most of the region. However, the magnified region at the edge step shows the spectra at a slightly lower energy as seen in the inset of Figure 5a. The pre-edge of the mixed material with Co = 2.4 shows only a single peak arising from the cubic structure with a slight shift to a higher energy. The main edge was also observed at a higher energy compared to that of the mixed material with Co = 1.2, due to the higher Co contents for both the 2^+ and 3^+ oxidation states. A relatively less intense pre-edge peak was observed for the Co K-edge of the mixed material with Co = 2.7, suggesting a less distorted octahedral structure. The main edge peak shifted to a higher energy compared to the XANES spectra of mixed materials with Co = 1.2 and 2.4, suggesting higher Co^{3+} contents in the mixed material with Co = 2.7.
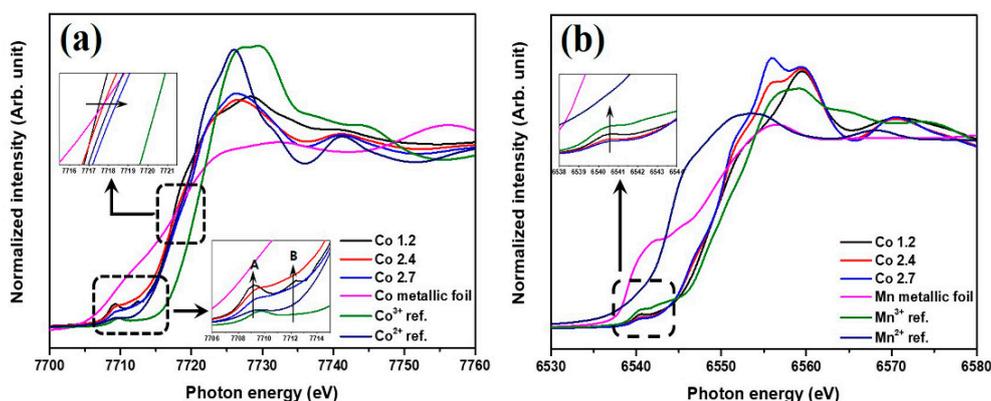
Figure 5. X-ray absorption near edge structure (XANES) (**a**) Co K-edge and (**b**) Mn K-edge spectra of Co- and Mn-based the mixed phase materials.

The Mn K-edge spectra for mixed materials with Co = 1.2, 2.4, and 2.7 are shown in Figure 5b along with Mn^0, Mn^{2+}, and Mn^{3+} reference spectra. The pre-edge of all the materials show less intense single peaks, as seen in the inset of Figure 5b. The main edge peak of the mixed material with Co = 1.2

was observed at a higher energy than the Mn^{2+} reference peak but a lower energy than the Mn^{3+} reference peak, presumably due to the presence of a mixture of cubic and tetragonal phases. The main edge peaks of other materials such as mixed materials with Co = 2.4 and 2.7 were found slightly at lower energies compared to the mixed material with Co = 1.2. This indicates that Mn retains ~3^+ oxidation states in all the materials but the local structure changes as inferred from the shape of the main edge peak on tuning the composition of materials.

Additionally, X-ray photoelectron spectroscopy (XPS) was performed on the samples to illustrate electronic configurations of the samples Figure 6. XPS analysis was performed on Co = 1.2, 2.4, and 2.7 to study the valence states of the cations. The C 1s peak at 284.6 eV was used as the reference peak for calibrating binding energies. The Co 2p spectra shows two main peaks at 780.0 and 795.0 eV, which are associated with the Co^{3+} $2p_{3/2}$ and $2p_{1/2}$ energy levels, respectively [22]. Two satellite peaks for the Co $2p_{3/2}$ and Co $2p_{1/2}$ states are present near at 788.0 and 802.0 eV, respectively. Additionally, the Co 2p spectra consist of two pair of spin orbit doublets and two shakeup satellites, which indicated the coexistence of Co 2^+ and 3^+ with the Co $2p_{3/2}$ and Co $2p_{1/2}$ energy levels Figure 6a–c.

The XPS spectra for the Mn 2p region show two major peaks at 642.0 and 653.0 eV, which are assigned to the binding energies of Mn^{3+} $2p_{3/2}$ and $2p_{1/2}$, respectively Figure 6d–f [22,23]. Notably, for Co = 1.2, Mn^{3+} $2p_{3/2}$ peak shows a shoulder near at 643.0 eV, which may be originated from Mn^{2+} in Mn_3O_4 phase as indicated by XRD result Figure 3. The high-resolution XPS spectra of the O1s is shown in Figure 6g–i, which was deconvoluted into three different peaks. The O 1s spectrum for Co- and Mn-based the mixed phase materials shows the main peak at around 529.80 eV, which can be attributed to lattice oxygens in M-O bonds, while the peaks at around 531.30 and 532.6 eV are associated with surface oxygens species and O-H groups, respectively [16,23,24]. Moreover, high amounts of the adsorbed O leads to high amounts of oxygen vacancies in the lattice, which results in an enhanced catalytic activity than the pristine lattice due to defective nature [25,26]. In the XPS spectra for Mn 2p, integrated peak area for the surface oxygen and O-H group peaks relative to the lattice oxygen peak was much larger for the mixed material with Co = 2.7 compared to those of Co = 1.2 and 2.4 Figure 6g–i. Hence, higher catalytic activity for OER can be expected for the Co- and Mn-based mixed phase material with higher Co content.

The electrocatalytic activity of mixed materials with Co = 1.2, 2.4, and 2.7 was evaluated using a typical three-electrode system with RDE in a 1 M KOH aqueous solution. Linear sweep voltammetry (LSV) was performed on all samples at a scan rate of 5 mV·s^{-1}. All potentials were iR-compensated to the reversible hydrogen electrode (RHE). LSV curves for the oxygen evolution reaction (OER) in 1.0 M KOH are shown in Figure 7a. The overpotential (η) required to deliver a current density of 10 mA·cm^{-2} (η^{10}) decreased with increasing Co content and the highest OER activity was observed for the mixed material with Co = 2.7. The η^{10} values of mixed materials with Co = 1.2, 2.4, and 2.7 were 490, 470, and 450 mV, respectively. The Tafel slope is a common metric for the kinetics of electrochemical reactions; a lower Tafel slope corresponds to faster reaction kinetics. The Tafel slopes for the η vs. log j plots were calculated as 44.2, 26.8, and 35.8 mV·dec^{-1} for mixed materials with Co contents of 1.2, 2.4, and 2.7, respectively Figure 7b. The mixed materials had comparable Tafel slopes in the range of 25–45 mV·dec^{-1}, indicating fast reaction kinetics during the OER. The LSV and Tafel slope data reveal that the OER catalytic performance of the mixed materials can be enhanced by increasing the Co content. Thus, a high content of Co^{3+} in the mixed materials is directly related to enhanced catalytic activity, which is an idea supported by XANES results. Overpotential for generating 10 mA cm^{-2} and Tafel slopes of the samples were compared with the recently reported transition metal based electrocatalysts, demonstrating a good electrocatalytic activity of our materials Table 1.
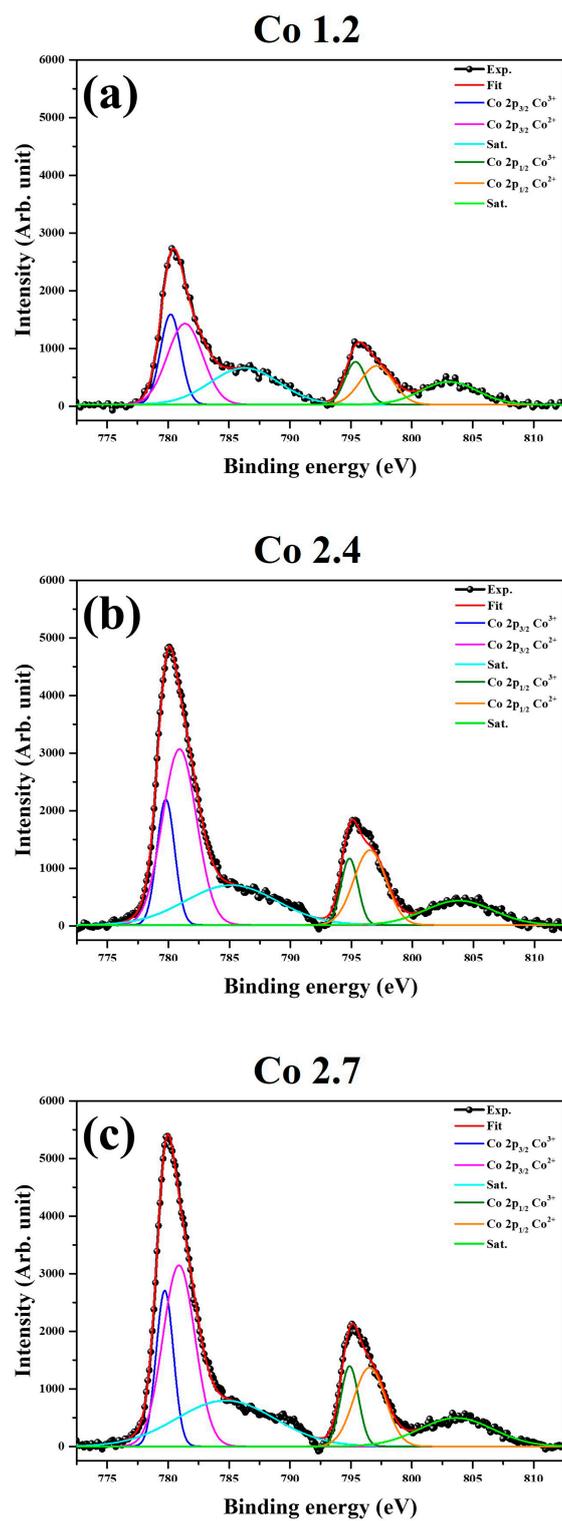
Figure 6. *Cont.*
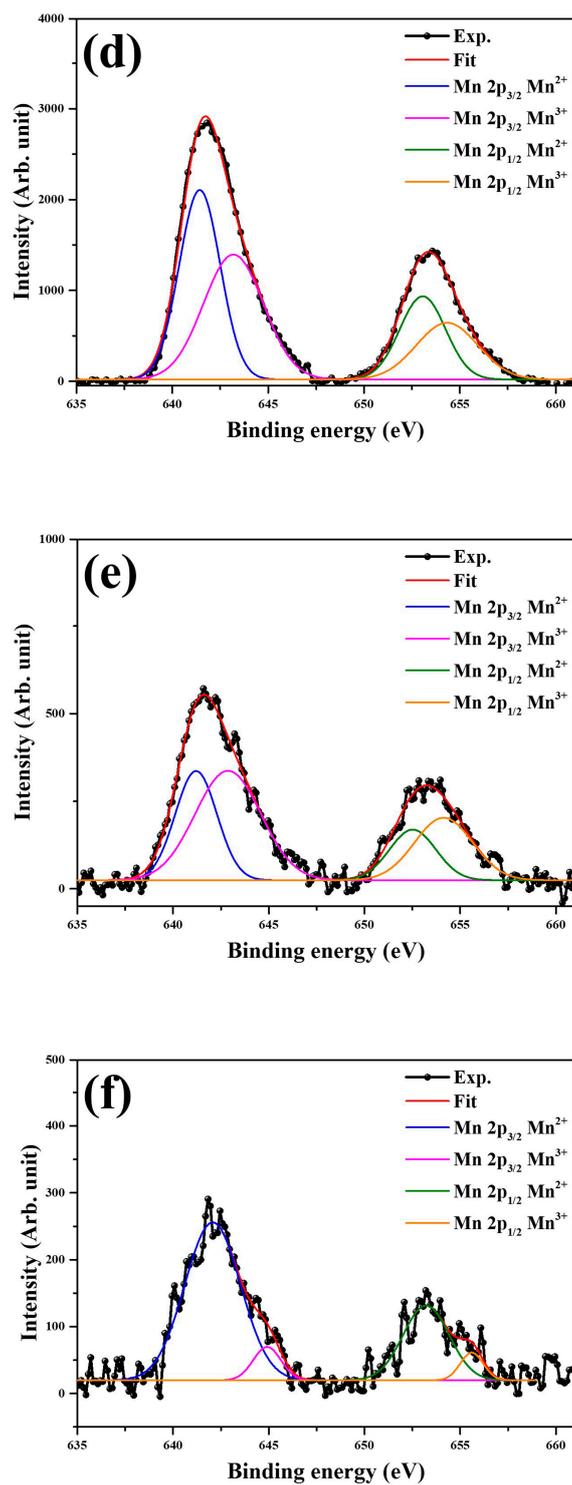
Figure 6. *Cont.*
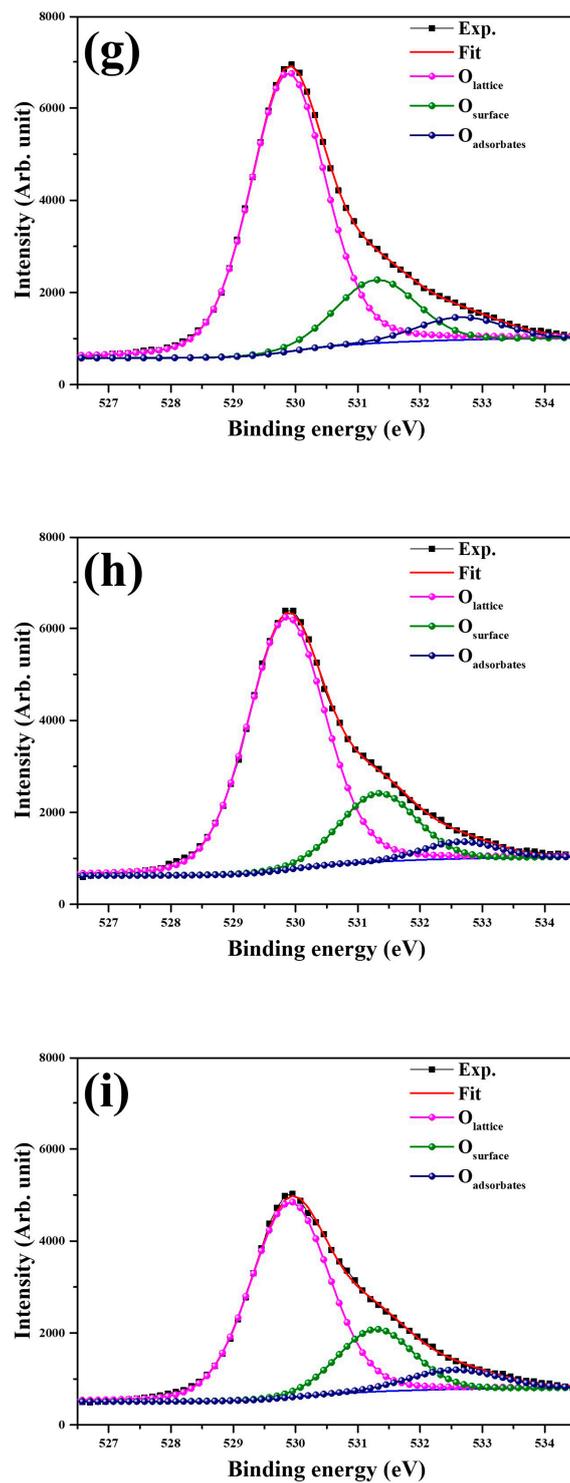
Figure 6. X-ray photoelectron spectroscopy (XPS) spectra of Co 1.2, Co 2.4, and Co 2.7 for Co 2p ((**a**), (**b**), and (**c**)), Mn 2p ((**d**), (**e**), and (**f**)) and O 1s ((**g**), (**h**), and (**i**)) orbitals with fitted lines, respectively.
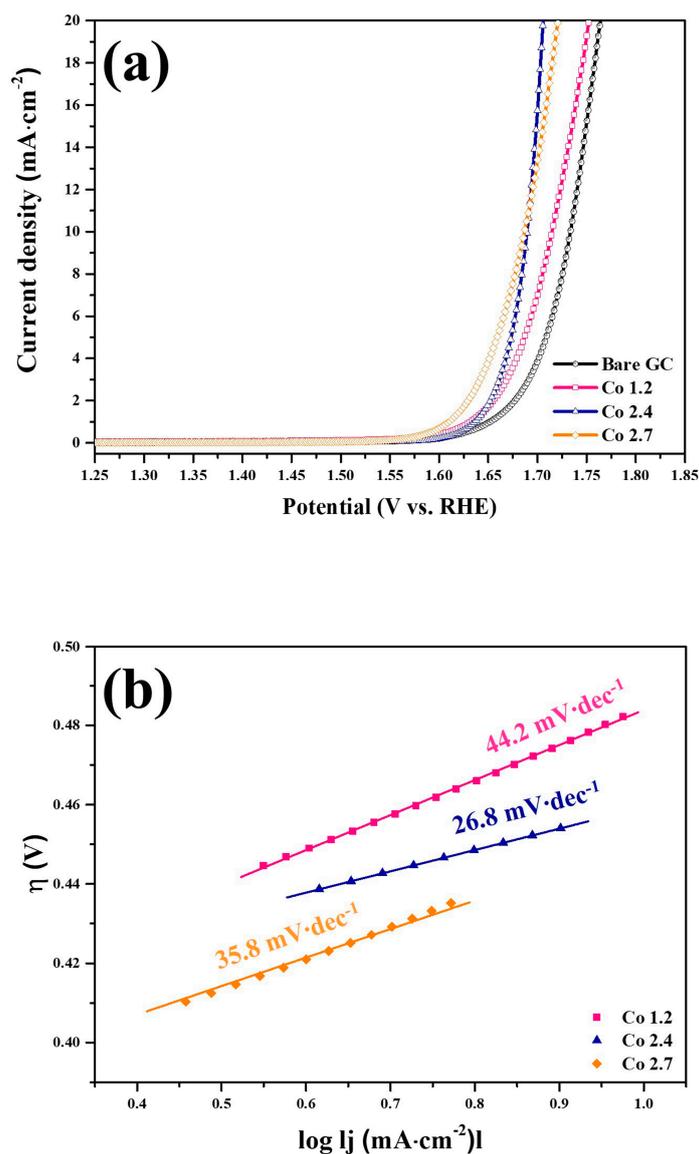
Figure 7. Electrochemical oxygen evolution reaction (OER) properties of Co- and Mn-based the mixed phase materials (Co = 1.2, 2.4 and 2.7). (**a**) Linear sweep voltammetry (LSV) polarization curves measured in 1.0 M KOH with a scan rate of 5 mV·s^{-1} and (**b**) corresponding Tafel plots.

Table 1. Comparison of OER catalytic activity of Co = 2.7 with that of other recently reported, transition metal-based catalysts.

Catalysts	Electrolyte	Current Density (mA cm^{-2})	Overpotential (mV)	Tafel Slope (mV dec^{-1})	References
Co- and Mn-based oxides	1 M KOH	10	450	35.8	This work
Mesoporous Co$_3$O$_4$	0.1 M KOH	10	411	80	[27]
CoO/CNT	1 M KOH	10	550	108	[28]
K$_{0.04}$[Co$_{0.42}$Mn$_{0.58}$O$_2$]	1 M KOH	10	420	110	[29]
Co$_3$O$_4$/MnCo$_2$O$_4$	0.1 M KOH	10	540	N/A	[30]
α-MnO$_2$-SF	0.1 M KOH	10	490	77.5	[31]
CoO/MoO$_x$	1.0 M KOH	10	490	44	[32]
Co$_2$B-500	0.1 M KOH	10	380	45	[33]
Ni$_x$B-300	1 M KOH	10	380	89	[34]
Co$_9$S$_8$@MoS$_2$/CNFs	1 M KOH	10	430	61	[35]
NiSe/NF	1 M KOH	10	400	N/A	[36]

Mixed phases of Co- and Mn-based materials with Co = 1.2, 2.4, and 2.7 were studied by EIS to calculate the R_{ct} of the catalysts. R_{ct} is generally determined from the semicircle diameter in the high-frequency region of a Nyquist plot (Z' vs. $-Z''$). Figure 8 shows the EIS data, using which the R_{ct} values were calculated as approximately 55, 50, and 45 Ω for mixed materials with Co = 1.2, 2.4, and 2.7, respectively. Notable, R_{ct} also decreased as the Co content increased, and the mixed material with Co = 2.7 showed the fastest electrical transport (i.e., the lowest R_{ct}) among the samples. This also implies that Co^{3+} plays an important role in facilitating the OER reaction kinetics. In addition, the ECSA of mixed materials with Co = 1.2, 2.4, and 2.7 was calculated using CV at different scan rates (20–120 mV·s^{-1}). The measured CV curves are presented in Figure 9. The scans were conducted over a voltage range of 1.31–1.41 V_{RHE}, where redox processes do not occur. This enabled measurement of the capacitive currents associated only with double-layer charging. The current density difference ($\Delta j = j_a - j_c$) at 1.36 V_{RHE} is plotted as a function of the scan rate in Figure 10, where the linear slope is equal to twice the double-layer capacitance (C_{dl}). The C_{dl} calculated from the fitted linear slopes were 0.291, 0.246, and 0.340 mF·cm^{-2} for mixed materials with Co = 1.2, 2.4, and 2.7, respectively. The ECSA of the mixed material with Co = 2.7 was the highest. In addition to good catalytic activity, long-term stability is an important requirement for practical applications of electrocatalysts. The electrocatalytic stabilities of mixed material with Co = 1.2, 2.4, and 2.7 were tested by chronoamperometric measurements at voltages, where a current density of 10 mA·cm^{-2} is generated. After 2 h of OER, the mixed material with Co = 1.2 showed a significant drop in the current density output (about more than 50%), indicating electrochemical degradation taking place during the OER Figure 11. In sharp contrast, as Co content increased, the stability improved remarkably. For the mixed material with Co = 2.4, no current drop was observed during 2 h of chronoamperometry Figure 11, demonstrating excellent stability in an alkaline solution. Furthermore, when the Co content increased up to 2.7, a large enhancement in the current density (about 40%) was observed after 2 h of OER, implying a boost in the catalytic activity of the mixed material with Co = 2.7 during the electrochemical reaction. The increased catalytic activity of mixed material with Co = 2.7 can be associated with the formation of cobalt hydroxide, $Co(OH)_2$, which is generally known as an active phase for the OER [37]. The oxidation of Co^{2+} to Co^{3+} can result in the increase of oxidative current at the beginning stage of chronoamperometry measurement in alkaline solution. A high amount of Co^{3+} in the mixed material with Co = 2.7 can facilitate the formation of $Co(OH)_2$ on the surface during the OER in alkaline media, resulting in an increased number of active sites. These results reveal that a high amount of Co^{3+} is desirable for increasing catalytic stability as well as activity in mixed materials synthesized by SCS.
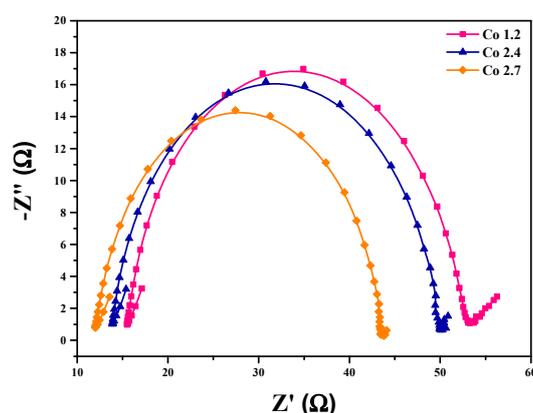
Figure 8. Nyquist plots of Co- and Mn-based the mixed phase materials (Co = 1.2, 2.4 and 2.7) in the frequency range from 0.1 to 100 kHz. A sinusoidal voltage with an amplitude of 5 mV was applied.
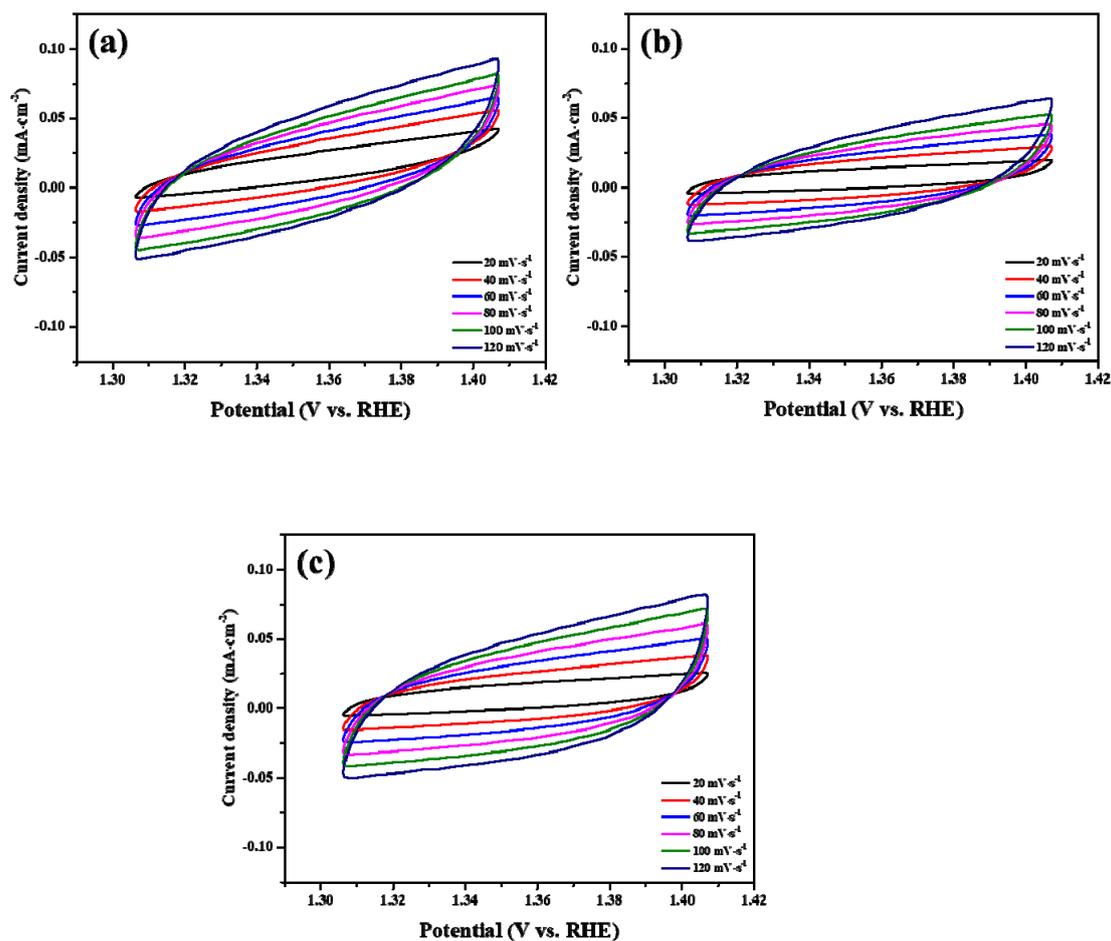
Figure 9. Cyclic voltammetry curves in a capacitive current region at various scan rates (20, 40, 60, 80, 100, and 120 mV·s^{-1}) of (**a**) Co 1.2, (**b**) Co 2.4, and (**c**) Co 2.4.
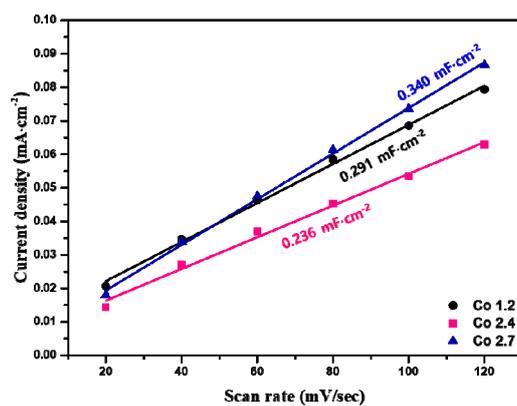
Figure 10. The current difference between anodic and cathodic sweeps as a function of scan rate for Co- and Mn-based the mixed phase materials (Co = 1.2, 2.4, and 2.7).
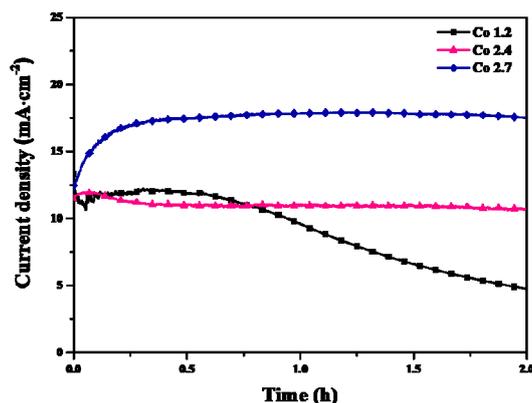
Figure 11. Chronoamperometry curve of Co- and Mn-based the mixed phase materials (Co = 1.2, 2.4, and 2.7) under an applied voltage where a current density of 10 mA·cm^{-2} is generated.

3. Experimental Section

3.1. Synthesis of CMO Powders

Manganese (II) nitrate (Mn(NO$_3$)$_2$; 50% aqueous solution), cobalt (II) nitrate hexahydrate (Co(NO$_3$)$_2$·6H$_2$O), citric acid (C$_6$H$_8$O$_7$), and ethylene glycol (C$_2$H$_6$O$_2$) were used as starting materials. First, stoichiometric amounts of Mn(NO$_3$)$_2$, Co(NO$_3$)$_2$·6H$_2$O, citric acid, and ethylene glycol were dissolved in distilled water. The molar ratio of nitrate to citric acid and ethylene glycol was maintained at 1:1:1. Ammonia solution was added to adjust the pH from 1 to 7. Heating at 80 °C transformed the solution into a sol. Subsequent heat treatment at 130 °C under constant stirring formed a brownish gel. Heating at 300 °C converted the gel into the mixed materials (as-received powder).

3.2. Structural Characterization

A transmission electron microscope (TEM, Talos F200X; Thermo Fisher Scientific) equipped with an energy dispersive X-ray (EDX) spectroscopy at 200 kV was used to study the microstructural structure of the mixed materials. X-ray diffraction (XRD, X'Pert-Pro MPD; PANalytical) measurements were conducted with Cu-K$_\alpha$ radiation (λ = 0.15418 nm) at 40 kV and 100 mA. Raman spectroscopy (LabRam HR; Horiba Jobin-Yvon) was performed for structural investigation of the mixed materials. X-ray photoelectron spectroscopy (XPS) (PHI 5000 VersaProbe; ULVAC-PHI, Enzo, Chigasaki, Japan) was carried out with pass energies of 100 and 20 eV for survey and high-resolution scans, respectively. The powder samples were analyzed for X-ray absorption spectroscopy (XAS) at the 7D beamline of Pohang Light Source (PSL-II). The 7D beamline is equipped with a double crystal monochromator (two sets of Si (111) crystals) and offers an energy resolution of 2 × 10^{-5}. A W metallic foil was used as the reference to calibrate the data. The data were processed using the ATHENA package (0.9.25, Naval Research Laboratory, Washington, DC, USA) [38].

3.3. Electrochemical Characterization

The electrochemical performance of Co- and Mn-based materials powder was evaluated in a 1 M KOH solution using a standard three-electrode electrochemical cell equipped with a rotating disk electrode (RDE). An electrochemistry potentiostation (PGSTAT302N; Metrohm) was used to record the electrochemical data. The working electrode was prepared as follows. Five miligrams of powder was well-dispersed in the solution (distilled water:ethanol = 3:1) with a Nafion® 117 solution (5 wt %) via ultrasonication for about 20 min. Then, 5 μL of the homogeneous solution was drop-cast onto a glassy carbon (GC) RDE with a diameter of 3 mm, which resulted in an approximate catalyst loading of 0.352 mg·cm^{-2}. The working electrode was dried overnight in air before the electrochemical characterization. The RDE was rotated at 2000 rpm to remove gas bubbles generated on the surface of the working electrode. The reference and counter electrodes were Ag|AgCl (3.5 M KCl) and Pt foil,

respectively. Linear sweep voltammetry (LSV) was performed at a scan rate of 5 mV·s^{-1} from 0.2 to 0.8 V vs. Ag|AgCl. All polarization curves were iR-corrected and calibrated against a reversible hydrogen electrode (RHE). The current density was normalized to the geometrical surface area and the measured potentials vs. Ag|AgCl were converted to a reversible hydrogen electrode (RHE) scale according to the Nernst equation.

$$E_{RHE} = E_{(Ag|AgCl)} + 0.0591 \times pH + 0.197 \tag{2}$$

Cyclic voltammetry (CV) was conducted to calculate the electrochemical effective surface area (ECSA) of the catalysts. It was performed in a potential window range of 1.31–1.41 V vs. RHE, where only capacitive currents flowed, at different scan rates (20, 40, 60, 80, 100, and 120 mV·s^{-1}) to estimate the electrochemical double-layer capacitance (C_{dl}). Electrochemical impedance spectroscopy (EIS) was performed over a frequency range of 0.1–100 kHz with a sinusoidal voltage (5 mV amplitude) to estimate the charge transfer resistance (R_{ct}).

4. Conclusions

Crystallographic information and OER performance related to it for mixed phases of Co- and Mn-based materials formed during solution combustion synthesis (SCS) undertaken for the formation of spinel (Co_xMn_{3-x})O_4 (CMO) were investigated. The mixed materials were prepared at 300 °C and further heat treatment was not performed at a higher temperature to synthesize mixed phases of CMO electrocatalysts. At low Co contents, low-crystalline CMO with a tetragonal spinel structure was observed with small amounts of Co_3O_4 and MnO phases. With increase in Co contents for up to 2.7, cubic spinel Co_3O_4 with CoO were observed. Raman spectra of the mixed materials also supported the hypothesis that low Co contents (Co = 1.2) lead to the formation of the tetragonal spinel CMO. With increase in the Co content to up to 2.7, Co_3O_4 was observed, wherein Co- rich and Mn-rich phases were completely separated. All mixed materials showed oxidation states of 2$^+$ and 3$^+$ for Co but an increase in the Co content resulted in higher oxidation states toward 3+, which can be attributed to the higher amount of Co_3O_4. As for catalytic activity, mixed materials with higher Co contents offered better OER performance including lower overpotentials, faster charge transfer, better reaction kinetics and stability owing to a greater amount of Co^{3+} being available, which facilitated the formation of $Co(OH)_2$ as an active phase for OER. Crystal structure dependent electrocatalytic properties of the mixed phases of Co- and Mn-based materials give insights for a new engineering concept for the next generation of OER electrocatalysts based on mixed phases.

Author Contributions: K.R.P. data curation, formal analysis, investigation, writing-original draft; J.E.J. data curation, formal analysis, investigation; G.A. investigation, methodology; Y.-H.K. data curation, investigation, methodology; H.H. data curation, formal analysis, writing-original draft, writing-review and editing; J.L. data curation, formal analysis, investigation; S.M. conceptualization, formal analysis, project administration, writing-original draft, writing-review and editing.

Funding: This research was funded by Korea Institute of Industrial Technology (KITECH), Republic of Korea, grant number JE190012. This research was funded by the Advanced Technology Center Association (ATCA), funded by the Ministry of Trade, Industry and Energy (MOTIE, Republic of Korea), grant number 10077336. This research was funded by Basic Science Research Program through the National Research Foundation of Korea (NRF) funded by the Ministry of Science, ICT & Future Planning, grant number 2018R1D1A1A02085938.

Conflicts of Interest: The authors declare no conflict of interest.

References

1. Amarilla, J.M.; Petrov, K.; Picó, F.; Avdeev, G.; Rojo, J.M.; Rojas, R.M. Sucrose-aided combustion synthesis of nanosized $LiMn_{1.99-y}Li_yM_{0.01}O_4$ (M=Al^{3+}, Ni^{2+}, Cr^{3+}, Co^{3+}, y = 0.01 and 0.06) spinels characterization and electrochemical behavior at 25 and at 55 °C in rechargeable lithium cells. *J. Power Sources* **2009**, *191*, 591–600. [CrossRef]

2. Manikandan, P.; Ananth, M.V.; PremKumar, T.; Raju, M.; Periasamy, P.; Manimaran, K. Solution combustion synthesis of layered $LiNi_{0.5}Mn_{0.5}O_2$ and its characterization as cathode material for lithium-ion cells. *J. Power Sources* **2011**, *196*, 10148–10155. [CrossRef]

3. Yu, P.; Zhang, X.; Chen, Y.; Ma, Y. Solution-combustion synthesis of ε-MnO_2 for supercapacitors. *Mater. Lett.* **2010**, *64*, 61–64. [CrossRef]

4. Jayalakshmi, M.; Balasubramanian, K. Solution combustion synthesis of Fe_2O_3/C, Fe_2O_3-SnO_2/C, Fe_2O_3-ZnO/C composites and their electrochemical characterization in non-aqueous electrolyte for supercapacitor application. *Int. J. Electrochem. Sci.* **2009**, *4*, 878–886.

5. Gupta, A.; Chemelewski, W.D.; Mullins, C.B.; Goodenough, J.B. High-rate oxygen evolution reaction on Al-doped $LiNiO_2$. *Adv. Mater.* **2015**, *27*, 6063–6067. [CrossRef] [PubMed]

6. Rai, A.K.; Gim, J.; Anh, L.T.; Kim, J. Partially reduced Co_3O_4/graphene nanocomposite as an anode material for secondary lithium ion battery. *Electrochim. Acta* **2013**, *100*, 63–71. [CrossRef]

7. Varma, A.; Mukasyan, A.S.; Rogachev, A.S.; Manukyan, K.V. Solution combustion synthesis of nanoscale materials. *Chem. Rev.* **2016**, *116*, 14493–14586. [CrossRef]

8. Erri, P.; Pranda, P.; Varma, A. Oxidizer-fuel interactions in aqueous combustion synthesis. 1. Iron(III) nitrate-model fuels. *Ind. Eng. Chem. Res.* **2004**, *43*, 3092–3096. [CrossRef]

9. Wen, W.; Wu, J.-M. Nanomaterials via solution combustion synthesis: A step nearer to controllability. *RSC Adv.* **2014**, *4*, 58090–58100. [CrossRef]

10. Merzhanov, A.G.; Rogachev, A.S. Structural macrokinetics of SHS processes. *Pure Appl. Chem.* **1992**, *64*, 941–953. [CrossRef]

11. Yu, Y.; Sun, C.; Yin, X.; Li, J.; Cao, S.; Zhang, C.; Voyles, P.M.; Wang, X. Metastable intermediates in amorphous titanium oxide: A hidden role leading to ultra-stable photoanode protection. *Nano Lett.* **2018**, *18*, 5335–5342. [CrossRef] [PubMed]

12. Sheng, J.; Li, Q.; Wei, Q.; Zhang, P.; Wang, Q.; Lv, F.; An, Q.; Chen, W.; Mai, L. Metastable amorphous chromium–vanadium oxide nanoparticles with superior performance as a new lithium battery cathode. *Nano Res.* **2014**, *7*, 1604–1612. [CrossRef]

13. Ge, X.; Liu, Y.; Goh, F.W.T.; Hor, T.S.A.; Zong, Y.; Xiao, P.; Zhang, Z.; Lim, S.H.; Li, B.; Wang, X.; et al. Dual-phase spinel $MnCo_2O_4$ and spinel $MnCo_2O_4$/nanocarbon hybrids for electrocatalytic oxygen reduction and evolution. *ACS Appl. Mater. Interfaces* **2014**, *6*, 12684–12691. [CrossRef]

14. Han, H.; Lee, J.S.; Ryu, J.H.; Kim, K.M.; Jones, J.L.; Lim, J.; Guillemet-Fritsch, S.; Lee, H.C.; Mhin, S. Effect of high cobalt concentration on hopping motion in cobalt manganese spinel oxide ($Co_xMn_{3-x}O_4$, x ≥ 2.3). *J. Phys. Chem. C* **2016**, *120*, 13667–13674. [CrossRef]

15. Han, H.; Lee, J.S.; Lim, J.; Park, K.R.; Kim, K.M.; Ryu, J.H.; Yeo, S.; Forrester, J.; Mhin, S. Synthesis of $Co_xMn_{1-x}O_4$ (0.9 ≤ x ≤ 2.7) nanopowders with controlled phase and composition via a gel-combustion method. *Ceram. Int.* **2016**, *42*, 17168–17173. [CrossRef]

16. Li, C.; Han, X.; Cheng, F.; Hu, Y.; Chen, C.; Chen, J. Phase and composition controllable synthesis of cobalt manganese spinel nanoparticles towards efficient oxygen electrocatalysis. *Nat. Commun.* **2015**, *6*, 7345–7352. [CrossRef]

17. Legutko, P.; Jakubek, T.; Kaspera, W.; Stelmachowski, P.; Sojka, Z.; Kotarba, A. Strong enhancement of deSoot activity of transition metal oxides by alkali doping: Additive effects of potassium and nitric oxide. *Top. Catal.* **2017**, *60*, 162–170. [CrossRef]

18. Widjaja, E.; Sampanthar, J.T.; Han, X.D.; Goh, E. Use of Raman microscopy and band-target entropy minimization technique to differentiate physical mixture from chemical mixture in mixed metal oxides. *Catal. Today* **2008**, *131*, 21–27. [CrossRef]

19. Hadjiev, V.G.; Iliev, M.N.; Vergilov, I.V. The Raman spectra of Co_3O_4. *J. Phys. C* **1988**, *21*, L199–L201. [CrossRef]

20. Gallant, D.; Pezolet, M.; Simard, S. Optical and physical properties of cobalt oxide films electrogenerated in bicarbonate aqueous media. *J. Phys. Chem. B* **2006**, *100*, 6871–6880. [CrossRef] [PubMed]

21. Jiang, J.; Li, L. Synthesis of sphere-like Co_3O_4 nanocrystals via a simple polyol route. *Mater. Lett.* **2007**, *61*, 4894–4896. [CrossRef]

22. Yu, L.; Zhang, L.; Wu, H.B.; Zhang, G.; Lou, X.W. Controlled synthesis of hierarchical $Co_xMn_{3-x}O_4$ array micro-/nanostructures with tunable morphology and composition as integrated electrodes for lithium-ion batteries. *Energy Environ. Sci.* **2013**, *6*, 2664–2671. [CrossRef]

23. Tang, Q.; Jiang, L.; Liu, J.; Wang, S.; Sun, G. Effect of surface manganese valence of manganese oxides on the activity of the oxygen reduction reaction in alkaline media. *ACS Catal.* **2014**, *4*, 457–463. [CrossRef]

24. Boosting electrochemical water oxidation through replacement of O_h Co sites in cobalt oxide spinel with manganese. *Chem. Commun.* **2017**, *53*, 8018–8021. [CrossRef] [PubMed]

25. Wang, Y.; Zhou, T.; Jiang, K.; Da, P.; Peng, Z.; Tang, J.; Kong, B.; Cai, W.; Yang, Z.; Zheng, G. Reduced mesoporous Co_3O_4 nanowires as efficient water oxidation electrocatalysts and supercapacitor electrodes. *Adv. Energy Mater.* **2014**, *4*, 1400696. [CrossRef]

26. Wang, H.Y.; Hung, S.F.; Chen, H.Y.; Chan, T.S.; Chen, H.M.; Liu, B. In operando identification of geometrical-site-dependent water oxidation activity of spinel Co_3O_4. *J. Am. Chem. Soc.* **2016**, *138*, 36–39. [CrossRef]

27. Sa, Y.J.; Kwon, K.; Cheon, J.Y.; Kleitz, F.; Joo, S.H. Ordered mesoporous Co_3O_4 spinels as stable, bifunctional, noble metal-free oxygen electrocatalysts. *J. Mater. Chem. A* **2013**, *1*, 9992–10001. [CrossRef]

28. Wu, J.; Xue, Y.; Yan, X.; Yan, W.; Cheng, Q.; Xie, Y. Co_3O_4 Nanocrystals on single-walled carbon nanotubes as a highly efficient oxygen-evolving catalyst. *Nano Res.* **2012**, *5*, 521–530. [CrossRef]

29. McKendry, I.G.; Thenuwara, A.C.; Shumlas, S.L.; Peng, H.; Aulin, Y.V.; Chinnam, P.R.; Borguet, E.; Strongin, D.R.; Zdilla, M.J. Systematic Doping of Cobalt into Layered Manganese Oxide Sheets Substantially Enhances Water Oxidation Catalysis. *Inorg. Chem.* **2018**, *57*, 557–564. [CrossRef]

30. Wang, D.; Chen, X.; Evans, D.; Yang, W. Well-dispersed Co_3O_4/Co_2MnO_4 nanocomposites as a synergistic bifunctional catalyst for oxygen reduction and oxygen evolution reactions. *Nanoscale* **2013**, *5*, 5312–5315. [CrossRef]

31. Meng, Y.; Song, W.; Huang, H.; Ren, Z.; Chen, S.; Suib, S. Structure–property relationship of bifunctional MnO_2 nanostructures: Highly efficient, ultra-stable electrochemical water oxidation and oxygen reduction reaction catalysts identified in alkaline media. *J. Am. Chem. Soc.* **2014**, *136*, 11452–11464. [CrossRef] [PubMed]

32. Yan, X.; Tian, L.; Atkins, S.; Liu, Y.; Murowchick, J.; Chen, X. Converting $CoMoO_4$ into CoO/MoO_x for overall water splitting by hydrogenation. *ACS Sustain. Chem. Eng.* **2016**, *4*, 3743–3749. [CrossRef]

33. Masa, J.; Weide, P.; Peeters, D.; Sinev, I.; Xia, W.; Sun, Z.; Somsen, C.; Muhler, M.; Schuhmann, W. Amorphous cobalt boride (Co_2B) as a highly efficient nonprecious catalyst for electrochemical water splitting: Oxygen and hydrogen evolution. *Adv. Energy Mater.* **2016**, *6*, 1502313. [CrossRef]

34. Masa, J.; Sinev, I.; Mistry, H.; Ventosa, E.; Mata, M.; Arbiol, J.; Muhler, M.; Cuenya, B.; Schuhmann, W. Ultrathin high surface area nickel boride (Ni_xB) nanosheets as highly efficient electrocatalyst for oxygen evolution. *Adv. Energy Mater.* **2017**, *7*, 1700381. [CrossRef]

35. Zhu, H.; Zhang, J.; Yanzhang, R.; Du, M.; Wang, Q.; Gao, G.; Wu, J.; Wu, G.; Zhang, M.; Liu, B.; et al. When cubic cobalt sulfide meets layered molybdenum disulfide: A core–shell system toward synergetic electrocatalytic water splitting. *Adv. Mater.* **2015**, *27*, 4752–4759. [CrossRef] [PubMed]

36. Tang, C.; Cheng, N.; Pu, Z.; Xing, W.; Sun, X. NiSe nanowire film supported on nickel foam: An efficient and stable 3D bifunctional electrode for full water splitting. *Angew. Chem. Int. Ed.* **2015**, *54*, 9351–9355. [CrossRef]

37. Koza, J.A.; Hull, C.M.; Liu, Y.C.; Switzer, J.A. Deposition of β-$Co(OH)_2$ films by electrochemical reduction of Tris(ethylenediamine)cobalt(III) in alkaline solution. *Chem. Mater.* **2013**, *25*, 1922–1926. [CrossRef]

38. Ravel, B.; Newville, M. ATHENA, ARTEMIS, HEPHAESTUS: Data analysis for X-ray absorption spectroscopy using IFEFFIT. *J. Synchrotron Radiat.* **2005**, *12*, 537–541. [CrossRef]